frontiers | Frontiers in Earth Science

ORIGINAL RESEARCH
published: 06 June 2022
doi: 10.3389/feart.2022.883836

Study of the Statistical Characteristics of Artificial Source Signals Based on the CSES

Jianping Huang[1,2], *Juan Jia*[2], *Huichao Yin*[3], *Zhong Li*[2]*, *Jinwen Li*[2], *Xuhui Shen*[1] and *Zeren Zhima*[1]

[1]National Institute of Natural Hazards, Ministry of Emergency Management of China, Beijing, China, [2]Institute of Intelligent Emergency Information Processing, Institute of Disaster Prevention, Langfang, China, [3]School of Information Engeering, Institute of Disaster Prevention, Langfang, China

The ground-based artificial source electromagnetic signal transmitted to space will form a pair of intensity regions over the station and its conjugate point. In order to study the position and intensity of the strongest points in the two regions, the power-spectrum density (PSD) of the electric field on board the Zhangheng-1 satellite (CSES) was selected when it passed over the NWC artificial source transmitting station. The selected frequency is centered at 19.8 kHz with a bandwidth of 200 Hz. The strongest point is defined as the location with the maximum power spectral density of ±10° around the NWC station within 5 days, which is the revisiting period of the CSES. The results show that statistical characteristics of strongest points vary as day/night, local/conjugate point, longitude/latitude, and different components of electric field vectors. In terms of longitude deviation, it is mostly westward offset at night and on both sides in the day over the NWC but opposite at the conjugate point. In terms of latitude deviations, it is equator-ward at night and the same during the day with a smaller deviation. While over the conjugate point, it is northward offset in the day and both at night with a bigger offset. In terms of intensity, it is stable without obvious seasonal changes over the NWC and its conjugate point. The intensity of PSD is higher at night than during the day. For the PSD intensity of the three components, the descending order over the NWC is Ead, Eab, and Ecd at night and Ecd, Ead, and Eab in the day, and the opposite is true for over the conjugate point.

Keywords: CSES, NWC station, conjugate point, electric power spectrum, statistical characteristics

OPEN ACCESS

Edited by:
Chao Xiong,
Wuhan University, China

Reviewed by:
Angelo De Santis,
Istituto Nazionale di Geofisica e Vulcanologia (INGV), Italy
Essam Ghamry,
National Research Institute of Astronomy and Geophysics, Egypt

***Correspondence:**
Zhong Li
lizhong@cidp.edu.cn

Specialty section:
This article was submitted to Environmental Informatics and Remote Sensing, a section of the journal Frontiers in Earth Science

Received: *25 February 2022*
Accepted: *19 April 2022*
Published: *06 June 2022*

Citation:
Huang J, Jia J, Yin H, Li Z, Li J, Shen X and Zhima Z (2022) Study of the Statistical Characteristics of Artificial Source Signals Based on the CSES. Front. Earth Sci. 10:883836. doi: 10.3389/feart.2022.883836

INTRODUCTION

When super large magnitude and shallow earthquakes occur, the energy of VLF electromagnetic waves will become stronger, resulting in space ionospheric disturbance, which is possibly useful for short-term strong earthquake prediction (Ni et al., 2013). One method to monitor ionospheric disturbances is to observe the propagation of artificially generated VLF (very low frequency, 3000–30000 Hz) electromagnetic signals in the lower ionosphere (Ni et al., 2019). Thus, scientists have deployed a number of ground-based artificial source transmitting stations around the world to continuously transmit VLF electromagnetic waves to space according to different frequencies. These signals can penetrate the ionosphere, propagate upward, and be reflected back to the ground and are synchronously received by satellites and ground receiving stations (Zhang et al., 2020). Although the energy of VLF electromagnetic waves emitted by artificial sources will decay

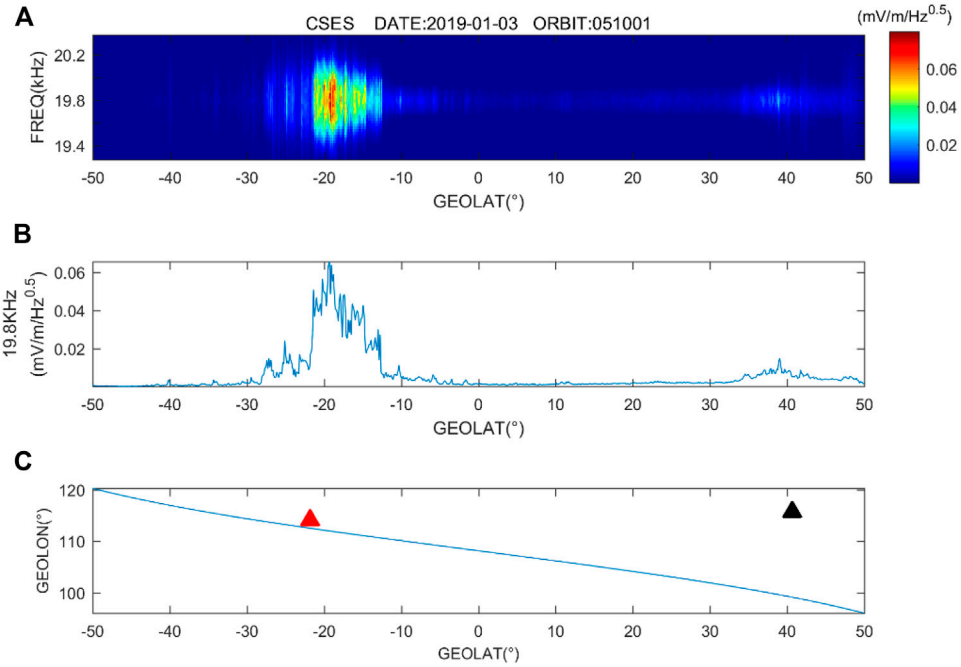

FIGURE 1 | Electric field PSD of the Eab component of the 051001 orbit.

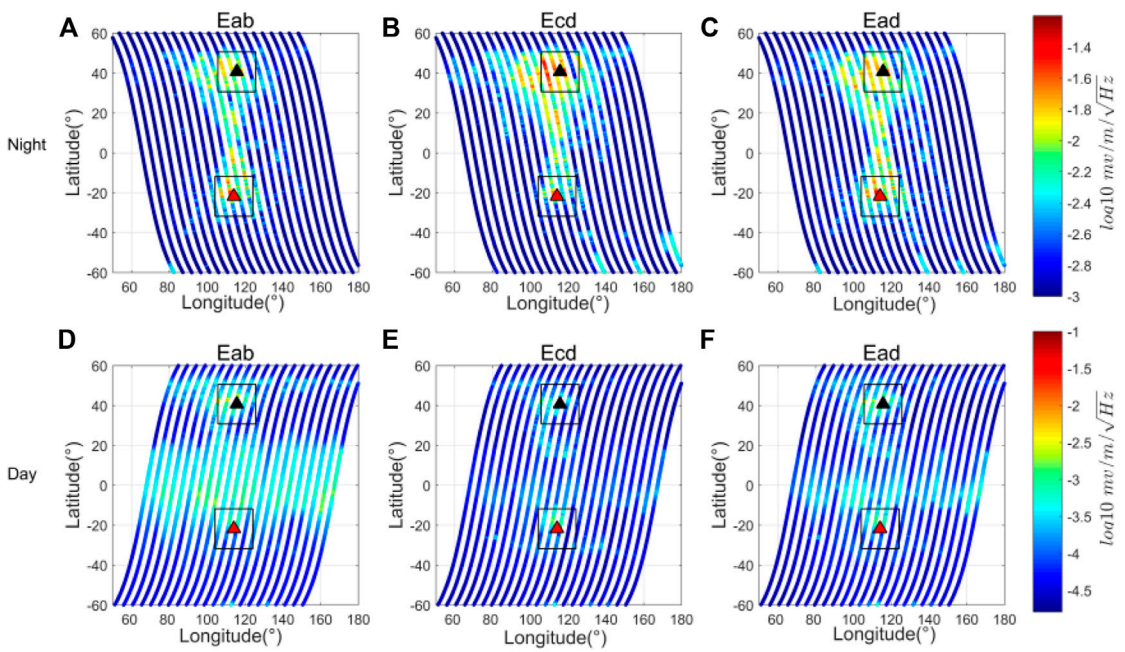

FIGURE 2 | Spatial distribution of the NWC signal in one cycle observed by the CSES (The abscissa is the geographic longitude, the ordinate is the geographic latitude, the color code is the PSD, and the red triangle and black triangle represent the projection position of the NWC station and its conjugate point on the ground, respectively. The first row **(A–C)** and the second row **(D–F)** represent the PSD distribution of the three components of the electric field on the nightside and the dayside, respectively.

while passing through the ionosphere (Lehtinen and Inan, 2009; Greninger and Colman, 2021), they generally show the characteristics of low energy loss and long transmission distance and can realize long-distance propagation in the earth ionospheric waveguide system. Moreover, it has obvious particle effects (Potirakis et al., 2018; Singh and Obara, 2020). When the

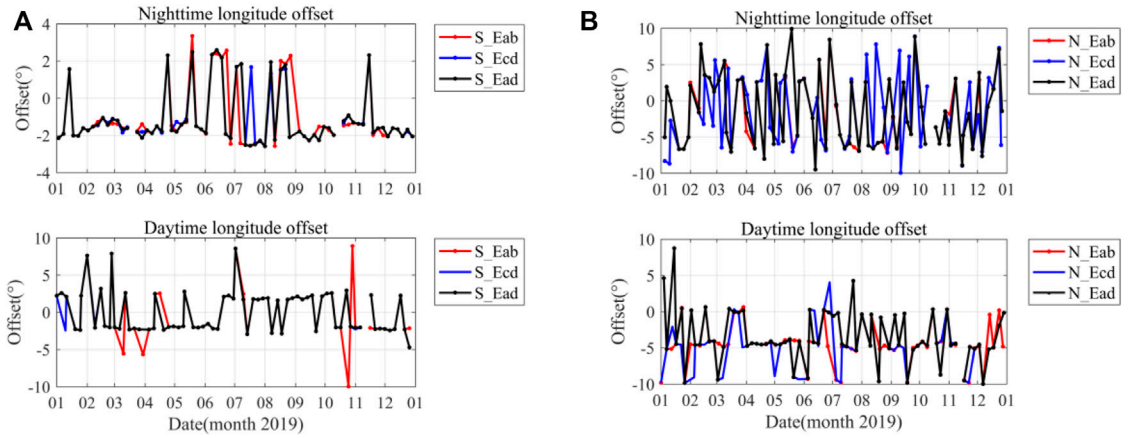

FIGURE 3 | Longitude shift of the strongest point of PSD of the electric field's three components.

satellite flies over the launch station, it can receive a stable artificial source signal in a specific frequency range. Due to the change in the velocity and phase of an electromagnetic wave when it propagates in the ionosphere, refraction, reflection, scattering, and other effects will also occur. Therefore, the electromagnetic response excited by the artificial source VLF signal in the ionosphere has temporal and spatial variation background characteristics of its own. The Australian NWC launching station (location: 21.82 S, 114.17 E, transmission frequency: 19.8 kHz, and transmission power: 1000 kW) is the only artificial source still in operation in the southern hemisphere (Li et al., 2014; Zhao et al., 2015). The transmitted VLF signal can produce a strong radiation effect on the ionosphere (Xu, 2016; Ivarsen et al., 2021).

On 2 February 2018, the China Seismo-Electromagnetic Satellite (CSES) dedicated to earthquake monitoring was launched; it is named "Zhangheng-1" and referred to as ZH-1. Its purpose is to establish a space test platform for monitoring the global space electromagnetic field, electromagnetic wave, ionospheric plasma, high-energy particle sedimentation, and other physical quantities and carry out electromagnetic monitoring of earthquakes above a magnitude of 7 in the world and above magnitude 6 in China (Shen et al., 2018). The CSES adopts a near-circular Sun-synchronous orbit divided into an ascending half orbit and a descending half orbit. The ascending one is the orbit of the satellite flying from south to north, and the descending one refers to the satellite flying from the north latitude to the southern latitude. The orbit is at an altitude of about 507 km, the inclination of about 97.4°, descending node at 14:00 LT, and the designed lifetime is 5 years. The revisit period is 5 days, and there will be 76 orbits in one revisit period (Yuan et al., 2018). The orbital distance in one period is between 4.7° and 4.8°. The CSES has two working modes: survey mode and burst mode. The CSES enters the burst mode when passing over China and the 1000 km area surrounding China or the global seismic belts, and in other areas, it is in the survey mode. The eight scientific payloads carried by the CSES are as follows: search coil magnetometer (SCM), high-precision magnetometer (HPM), electric field detector (EFD), GNSS occultation receiver, plasma analyzer package, high-energy particle detector, Langmuir probe, and tri-band beacon transmitter (Wang et al., 2016; Lu et al., 2017). Among them, the EFD adopts a dual-probe mode and calculates the electric field by obtaining the electric potential difference between two points in space. On the CSES, there are four 4.5-m-long extension rods. The end has a 60 mm diameter coating ball (respectively called a, b, c, and d), forming a tetrahedral structure.

The space vector electric field strength is obtained based on the electric potential difference in three directions and the corresponding distance between two balls. The detection frequency band is divided into ULF (0–16 Hz), ELF (6 Hz–2.2 kHz), and VLF (1.85 kHz-20 kHz) 、HF (18 kHz-3.5 MHz) (Ma et al., 2018). Among them, the sampling rate of VLF is 50 kHz, and its sampling period is 40.96 ms; thus, there are 2048 sampling points in each period. Because of the storage and downlink onboard the CSES, the duty ratio is 50% (Huang et al., 2018).

This study uses the electric field power spectrum density data detected by the EFD to study the characteristics of the maximum power spectrum density (MPSD) over the NWC station and the conjugate point and compares the statistic characteristics in the longitude offset, latitude offset, intensity of regional MPSD over NWC, and its conjugate point.

Data Selection

Using the single-component PSD of the electric field VLF band recorded by the French DEMETER satellite, several earthquake researchers have conducted in-depth research on the phenomenon of ionospheric disturbance before the earthquake and obtained some understandings, such as the similarity of power-spectrum morphology in different periods, the enhancement of electric field intensity on the nightside, and so on (Zhu, 2010; Yao et al., 2011; Shufan et al., 2016; Yang et al., 2018; Meredith et al., 2019). In addition, the change in high-energy electrons in the ionosphere caused by NWC is found by PROBAV and the nightside is stronger than the dayside (Cunningham et al., 2020). Based on DEMETER's findings, the distribution range of the strongest electric field

TABLE 1 | Comparison of the longitude offset of the three-component strongest point over the NWC and its conjugate point.

	Δlon	*count*	*|min|*	*|max|*	*|mean|*	*std*
S_Eab_night	>0	13	1.56	3.34	2.21	0.45
	<0	59	1.06	3.84	1.82	0.46
S_Ecd_night	>0	13	1.33	2.59	1.95	0.43
	<0	59	0.92	6.4	1.83	0.71
S_Ead_night	>0	12	1.52	2.59	2.05	0.37
	<0	60	0.92	3.84	1.81	0.46
S_Eab_day	>0	32	1.58	8.9	2.95	2.07
	<0	39	1.56	9.97	2.56	1.46
S_Ecd_day	>0	31	1.58	8.56	2.73	1.81
	<0	40	1.56	4.72	2.26	0.49
S_Ead_day	>0	32	1.58	8.56	2.73	1.78
	<0	39	1.56	4.72	2.26	0.49
N_Eab_night	>0	28	1.25	8.89	4.09	2.27
	<0	44	0.02	9.49	4.98	2.36
N_Ecd_night	>0	31	0.41	8.89	4.13	2.4
	<0	41	0.5	9.94	5.21	2.28
N_Ead_night	>0	29	1.25	9.92	4.27	2.48
	<0	43	0.02	9.49	4.86	2.41
N_Eab_day	>0	7	0.03	0.62	0.36	0.23
	<0	64	0.14	9.98	4.91	2.34
N_Ecd_day	>0	7	0.16	4.04	0.81	1.43
	<0	64	0.13	9.98	5.44	2.67
N_Ead_day	>0	12	0.17	8.75	1.71	2.73
	<0	59	0.06	9.98	4.49	2.71

radiation area over the NWC showed that the area with strong day–night and day-side radiation of the NWC is located on the equator side, and the conjugate area also has an enhanced electric field radiation area (Cohen et al., 2012; Cohen and Inan, 2012; Němec et al., 2020), and the effect of thermionic temperature enhancement was found over NWC and conjugated regions (Bell et al., 2011).

In summary, the areas of electric field disturbances over the NWC and its conjugate point are studied based on DEMETER's findings, and there is a lack of research on the temporal and spatial distribution characteristics of the maximum electric field power spectrum over the NWC and conjugate point. Since the DEMETER satellite had fallen in 2010, this study uses the electric field PSD recorded by the CSES to explore the deviation of the latitude and longitude of the strongest point in each cycle and the variation of the strongest point. The PSD of the electric field VLF band comprises three components, Eab, Ecd, and Ead, which are collected by three pairs of probes ab, cd, and ad, respectively (Gao et al., 2021). While studying the electric field ULF band waveform data, it is found that the performance characteristics of the three components of the electric field are inconsistent (Li et al., 2022), which provides a reference for this study. Since the frequency of the NWC transmitting station is 19.8kHz, with a bandwidth of 200 Hz, the VLF PSD with 19.8 kHz ± 200 Hz of EFD onboard the CSES is extracted for statistical analysis.

The Spatial Distribution Characteristics of PSD

When the electromagnetic satellite passes over the NWC station and its conjugate point, the electric field PSD peaks due to signal resonance. By observing the PSD curve of the three components of the electric field, it is found that the position and intensity of the wave crest change with time, and the variation characteristics of each component are also different. Taking the Eab component as an example, the PSD of an orbit passing directly over the NWC station from south to north is shown in **Figure 1**. An obvious spectral line in **Figure 1A** is the signal of the NWC transmitting station (frequency is 19.8 KHz), **Figure 1B** shows the variation diagram of the PSD value corresponding to the NWC station with latitude. **Figure 1C** shows the orbital position passing over the NWC, the red triangle represents the position of the NWC station, and the black triangle represents the position of the conjugate point. As can be seen from **Figure 1**, wave peaks appear within 10° of latitude near the NWC station and its conjugate point. The peak value and the corresponding spatial position are regarded as the information of the strongest point of the electric field power spectrum. Due to different satellite orbit intervals and different distances to the NWC station in a cycle, the search for the MPSD will produce large errors. Therefore, taking the operation cycle as a single unit, the distribution characteristics of the strongest points of the PSD at the NWC station and its conjugate points are studied.

The VLF band electric field three-component PSD of the NWC station from 6 January 2019 to 10 January 2019 is selected to obtain the PSD of the spatial orbit distribution diagram of electric field power spectrum intensity of 19.8 khz VLF band on the nightside and dayside in a cycle, as shown in **Figure 2**.

As can be seen from **Figure 2**, between 50°S ~ 50°N in latitude and 110°E ~ 130°E in longitude, there are two local strongest regions at Ecd and Ead components during the day and all three components in the night, while the Eab component on the dayside is the local strongest area. From the perspective of distribution, the local strongest area and MPSD intensity of the three components on the nightside are larger than those on the dayside. On the nightside, the PSD of the three components over the NWC station is greater than that over the conjugate area, while the Ecd component is the opposite; On the dayside, the PSD of the three components near the equator is significantly enhanced, and there is also a significant effect over its conjugate point; the strongest areas on the nightside and the dayside are concentrated within 10° above the NWC station and the conjugate point, and the strongest points of the NWC are concentrated near the equator, and the strongest points at the conjugate point are concentrated to its northwest.

In order to further analyze the variation trend of the local strongest point over time and in the three components, it is necessary to continue extracting the information of the strongest point of each cycle in 2019 for spatiotemporal analysis.

The Position and Amplitude Variation Characteristics of the Strongest Point of PSD

Using the VLF signal PSD in the 10° range near the NWC (southern hemisphere) station and its conjugate point (northern

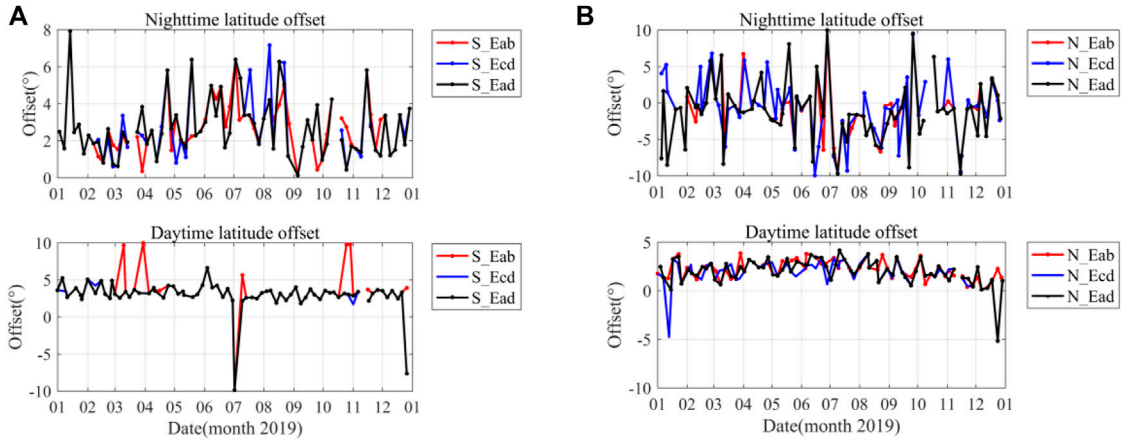

FIGURE 4 | Latitude offset of the strongest point of the three components of the electric field.

TABLE 2 | Comparison of the latitude offset of the three-component strongest point over the NWC and its conjugate point.

	Δlat	*count*	*|min|*	*|max|*	*|mean|*	*std*
S_Eab_night	>0	71	0.13	7.91	2.67	1.44
	<0	1	9.36	9.36	9.36	0.00
S_Ecd_night	>0	72	0.13	7.91	2.75	1.75
	<0	0	Null	Null	Null	Null
S_Ead_night	>0	71	0.13	7.91	2.71	1.6
	<0	1	9.36	9.36	9.36	0
S_Eab_day	>0	70	1.81	9.96	3.74	1.72
	<0	1	9.87	9.87	9.87	0
S_Ecd_day	>0	69	1.69	6.60	3.23	0.83
	<0	2	7.65	9.87	8.76	1.57
S_Ead_day	>0	69	1.81	6.60	3.26	0.84
	<0	2	7.65	9.87	8.76	1.57
N_Eab_night	>0	23	0.10	10.00	3.06	3.07
	<0	49	0.03	9.70	3.38	2.92
N_Ecd_night	>0	28	0.28	10.00	3.31	2.85
	<0	44	0.30	9.95	3.20	3.15
N_Ead_night	>0	20	0.28	10.00	3.62	3.14
	<0	52	0.03	9.70	3.29	2.87
N_Eab_day	>0	71	0.10	3.86	2.18	0.96
	<0	0	Null	Null	Null	Null
N_Ecd_day	>0	69	0.10	3.79	2.04	0.89
	<0	2	4.77	5.17	4.97	0.28
N_Ead_day	>0	70	0.09	4.16	2.09	0.97
	<0	1	5.17	5.17	5.17	0.00

hemisphere), that is, (11.82 S–31.82 S; 104.17 E ~ 124.17 E) and (30.647–50.647 N; 105.692 E ~ 125.692 E), the position of the strongest point of the PSD value and the characteristics of PSD changing with time in each cycle on the nightside and dayside of the three components are studied. The calculation formulas of the longitude offset and latitude offset are as follows:

$$\Delta lon = lon\_obs - lon\_sta. \quad (1)$$

$$\Delta lat = lat\_obs - lat\_sta. \quad (2)$$

Among them, lon_obs represents the longitude of the strongest point, lon_sta represents the longitude of the NWC station or its conjugate point, Δlon represents the longitude offset, lat_obs represents the latitude of the strongest point sought, lat_sta represents the latitude of the NWC station or its conjugate point, and Δlat represents the latitude offset quantity.

Longitude Variation Characteristics of the Strongest Point of PSD

The variation characteristics of the longitude of the strongest point of the electric field PSD in each cycle are calculated by **formula (1)**, as shown in **Figure 3**. The longitude offset of the strongest point of the NWC station is shown in **Figure 3A**, in which the longitude offset of the three components on the nightside is within [−2°,2°], and most of the data are offset to the west of the NWC station by about 2°. From April to August and November, three components began to offset to the east of the NWC station, and the offset exceeded 2°. The longitude offset of most of the data on the three components on the dayside is within [−2°,2°], and the longitude offset to the east of the NWC station is more than 5° in February, July, and November. The offset of the Eab component is significantly different from that of the other two components in March and October, and its offset to the NWC station exceeds 5°.

The longitude offset of the strongest point of the conjugate point is shown in **Figure 3B**, in which the longitude offset of the three components on the nightside is within [0°,10°], and most of the data of the three components are relatively evenly offset to the east and west sides of the conjugate point, with a range of [− 5°,5°]; the longitude offset of the three components on the dayside is within [−10°,10°], and most of the data are offset to about 5° to the west of the conjugate point.

It can be seen that the longitude offset of the three strongest points of the NWC station is generally distributed on the west side on the nightside and relatively evenly distributed on the east and west sides on the dayside; The longitude offset at the conjugate point is mainly concentrated in the range of 5° on east and west sides on the nightside and near 5° on the west side on the dayside.

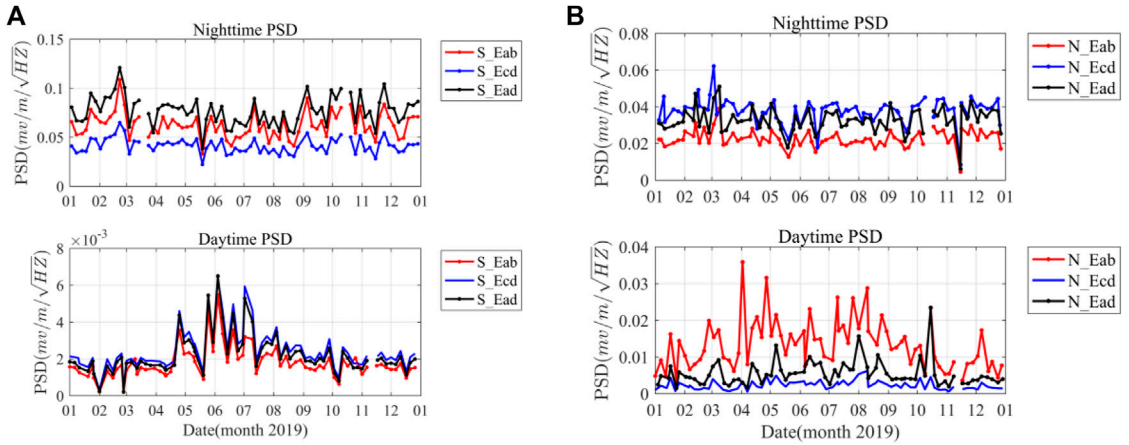

FIGURE 5 | Variation characteristics of MPSD.

TABLE 3 | Comparison of the annual average power spectrum values of the three-component strongest point over the NWC and its conjugate point.

		Night (mv/m/HZ ^ 0.5)			Day (mv/m/HZ ^ 0.5)		
		Ecd	Ead	Eab	Ecd	Ead	Eab
NWC	*|mean|*	0.0626	0.0414	0.0769	0.0018	0.0024	0.0022
	std	0.0132	0.0075	0.0149	0.0009	0.0011	0.0011
Conjugate point	*|mean|*	0.0225	0.0377	0.0327	0.0134	0.0023	0.0054
	std	0.0048	0.0072	0.0068	0.0068	0.0012	0.0034

The comparison results of the longitude offsets of the strongest point of the three-component PSD of the electric field over the NWC station and its conjugate points in 2019 on the dayside and nightside are shown in **Table 1**, where $|min|$ represents the absolute value of the minimum offset, $|max|$ represents the absolute value of the maximum offset, $|mean|$ represents the absolute value of the average offset, std is the mean square deviation of the offset, the count represents the number of points in this range, *S* represents the NWC station, *N* represents its conjugate point, and S_Eab_night represents the nightside Eab component value of the NWC station, and other variables are analogized meanings.

The Eab component is taken as an example from **Table 1**:

1) Considering the longitude shift of the strongest point of the PSD, it is biased to the west over the NWC station, and the nightside (accounting for more than 80%) is more obvious than the dayside (accounting for slightly more than 55%); over the conjugate point, it is also biased to the west, and the dayside (accounting for more than 88%) is stronger than the nightside (accounting for more than 56%), which is contrary to the diurnal characteristics over the NWC station. The other two components have similar characteristics.
2) Considering the offset range of the strongest point of the PSD, the offset range of the east and west sides over the NWC station is within [1°, −4°]; the average value of the east offset is greater than that of the west, and the offset range and average value of the dayside are greater than those of the nightside. Over the conjugate point, the offset range of the east and west sides is between [0°, 10°] and the east offset range and the average value of the dayside are much smaller than those of the nightside, while the west offset range and the average value of the dayside and nightside have minor differences; the average value of eastward migration is less than that of westward migration, which is contrary to the situation over the NWC station, with its migration range being larger. The performance characteristics of the other two components are similar to those of this component.
3) Analyzing the stability of longitude migration data, the stability of nightside data over the NWC station is greater than that of the dayside and the stability of the dayside and nightside data over the conjugate point is similar. In general, the stability of the data over the NWC station is greater than that of its conjugate point, and the stability of the other two components is similar.

Latitude Variation Characteristics of the Strongest Point of PSD

The time-varying characteristics of the latitude of the strongest point of the electric field PSD in each cycle are shown in **Figure 4** in which **Figures 4A,B**, respectively, represent the latitude offset over the NWC station and its conjugate point. As can be seen from **Figure 4A**, the offset to the equator side of the three components on the nightside is between 0° and 6°,

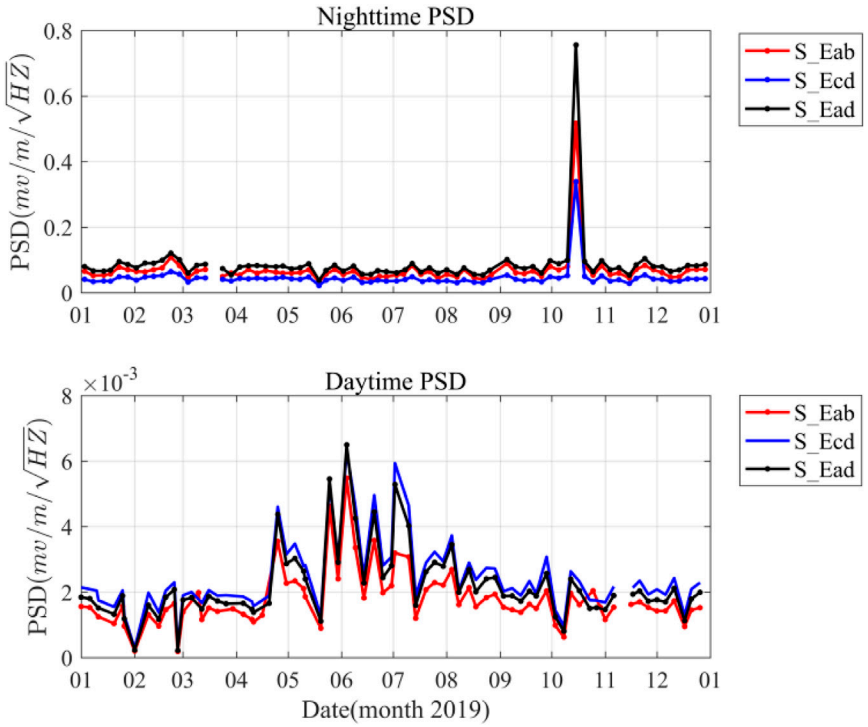

FIGURE 6 | Abnormal change characteristics of the PSD of the strongest points on the night and daysides of the magnetic conjugate point.

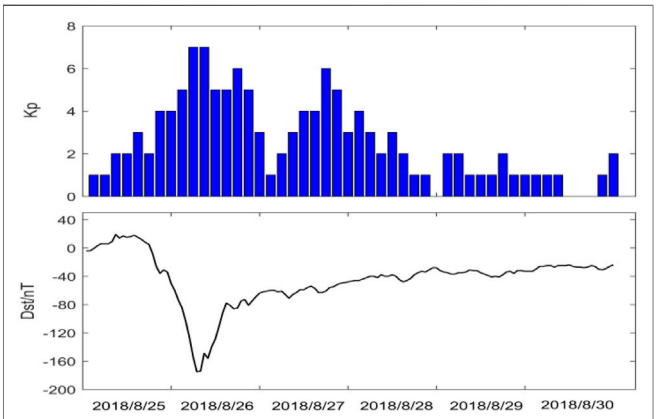

FIGURE 7 | Variation of geomagnetic indexes Kp and Dst.

showing an increasing trend from June to August, and the offset of the Ecd component exceeds 6°. The three components on the dayside are mainly offset to the equatorial side, with an amplitude of 2°–5°. The offset of the Eab component to the equatorial side is more than 5° in March, April, and October, and the three components are offset to the south of the NWC station in July and December and all for more than 5°.

As can be seen from **Figure 4B**, most of the data of the three components on the nightside are evenly shifted to the north and south sides of the conjugate point, with an amplitude of [– 5°, 5°]. From June to September, the data are mainly shifted to the south of the conjugate point. Most of the data of the three components on the dayside are offset to the north of the conjugate point, with an amplitude of [0°, 5°]. The Ecd and Ead components are offset to the south of the conjugate point by nearly 5° in January and December, respectively.

It can be seen that the latitude offset of the three components of the NWC station is mainly distributed in the north, and only very few points on the dayside are distributed in the south. The latitude offset of the three components of the conjugate point is distributed on the north and south sides on the nightside and mainly on the north side on the dayside. The latitude offset on the three components of the NWC station and conjugate point is compared and analyzed. The offset direction on the nightside is inconsistent, and the offset on the dayside is mostly on the north side.

The latitude shift results of the strongest points of the electric field PSD in 2019 are listed in **Table 2**, and the meaning of each parameter is shown in **Table 1**.

Still, taking the Eab component as an example to discuss

1) Considering the latitude offset of the strongest point of the PSD, when it is over the NWC station, its latitude is mainly biased to the north (more than 95%); over the conjugate point, the daytime latitude is biased to the north (more than 98%) and the nighttime latitude is mainly biased to the south (more than 60%). The offset direction of the other two components is similar to the day and night characteristics of the Eab component.
2) To analyze the latitude offset range, while over the NWC station, the offset range and average value on the north side of the dayside are greater than those of the nightside. Over the

conjugate point, the offset range and average value on the north side of the nightside conjugate point are greater than those on the dayside. and the other two components are similar to this component.

3) To analyze the stability of latitude migration, the migration stability over the NWC station is better, the stability of nightside is greater than that of the dayside, and the opposite is found over the conjugate point. The stability of the other two components also has similar characteristics.

Variation Characteristics of Electric Field MPSD Amplitude

The statistics of the intensity of electric field MPSD in each operation cycle in 2019 are shown in **Figure 5**, in which **Figures 5A,B** represent the variation diagram of the intensity of MPSD at the NWC station and its conjugate point, respectively.

As can be seen from **Figure 5A**, over the NWC station, the MPSD of the three components on the nightside is between 0.04 and 0.12 mv/m/Hz ^0.5 and meets the relation Ead > Eab > Ecd; the MPSD of the three components on the dayside is between 0 and 0.007 mv/m/Hz ^0.5, showing an increasing trend from May to July and meets the relation: Ecd > Ead > Eab.

As can be seen from **Figure 5B**, the MPSD of the three components on the nightside is mainly distributed between 0.02 and 0.05 mv/m/Hz ^0.5 above the conjugate point and meets the relation: Ecd > Ead > Eab. The MPSD of the three components on the dayside is mainly distributed between 0 and 0.025 mv/m/Hz^ 0.5 and meets the relation: Eab > Ead > Ecd.

The changes in the MPSD of the three components with time in each cycle are similar such that they increase or decrease at the same time. The change range of the nightside is small and that of the dayside is large.

The comparison of annual average values of three component MPSD of the NWC station and its conjugate points is shown in **Table 3**.

It can be seen from **Table 3** that the mean value of the MPSD of the NWC station and its conjugate point on the three components on the nightside is greater than that on the dayside and that of the NWC station is much greater than that of its conjugate point. On the diurnal side, that of the conjugate point is larger than that of the NWC station, and only the Ecd component has the opposite effect. To analyze the data stability, the stability over the conjugate point on the nightside is greater than that of the NWC station, while on the dayside, it is the opposite.

CONCLUSION AND DISCUSSION

Based on the VLF band PSD of the electric field recorded by the CSES from January to December 2019, taking the NWC artificial source transmitting station and the 10° range near its conjugate point as the research area, this study includes a statistical analysis of the temporal and spatial variation of the strongest point in each cycle and obtains some understanding of the variation law of spatial electric field intensity with time.

DISCUSSION

The MPSD of the three components in each cycle over the NWC station and its conjugate points is different, which may be related to the direction of the satellite or the type of orbit. There is an abnormal sudden change value in the nightside MPSD in October 2019, as shown in **Figure 6**. However, Dst ≤ -100 and Kp > 5 occurred on August 26 and 27, 2018. It is estimated that a large magnetic storm occurred during this period (Liao et al., 2018; Zhu et al., 2021), as shown in **Figure 7**, and the MPSD in these 2 days has reached 0.05 mv/m/Hz ^0.5, which is far less than the abnormal abrupt mutation value. It is speculated that the abnormal value abrupt value change in October 2019 has no obvious relationship with the magnetic storm. It is necessary to analyze whether the MPSD value variation is related to the earthquake in subsequent work.

CONCLUSION

There Are Four Main Conclusions

1) In terms of longitude, most of the three components of the nightside of the NWC station are mainly offset to the west, and those on the dayside is offset on its east and west sides; on the nightside of the conjugate point, the strongest points of the three-component PSD are offset to the east and west and those on the dayside is mainly offset to the west, and the offset of the conjugate point is greater than that of the NWC station.

2) In terms of latitude, the strongest points of the PSD of the three components in the NWC station are all biased to the north, the offset amplitude of the nightside increases with time, and the offset amplitude of the dayside tends to be stable, but the Eab component has an abnormal offset in March and October, and the amplitude reaches 10°. The strongest points of the nightside at the conjugate point are offset on the south and north sides, the diurnal side is offset to the north, and the offset amplitude of the nightside is larger than that of the dayside.

3) On the nightside of the NWC station, the variation range of the MPSD of the three components is stable, and there are no obvious seasonal characteristics. and it meets the order: Ead > Eab > Ecd; The variation of MPSD on the dayside has an obvious increase from May to July, and it meets the order: Ecd > Ead > Eab; The variation range of MPSD on the nightside of the conjugate point is stable, there are no obvious seasonal characteristics, and it meets the order: Ecd > Ead > Eab; The MPSD variation amplitude of the Eab component on the dayside is greater than that of the other two components, and it meets the order: Eab > Ead > Ecd; The MPSD of different components on the nightside and the dayside is obviously different, and the nightside is all greater than that on the dayside.

4) Over the NWC station and its conjugate point, the longitude offset, latitude offset, and MPSD value of the strongest point in PSD in each cycle have similar variation shapes with time, and

these three parameters change more obviously every month at the NWC station than at its conjugate point.

DATA AVAILABILITY STATEMENT

The datasets presented in this study can be found in online repositories. The names of the repository/repositories and accession numbers can be found below: www.leos.ac.cn.

AUTHOR CONTRIBUTIONS

JH contributed to the conception and design of the study, JJ contributed to model construction, ZL contributed to the methodology, HY contributed to the editing and typesetting, and JL contributed to data analysis, XS and ZR contributed to writing. All authors approved the final manuscript.

FUNDING

This research was funded by Dragon 5 cooperation Proposal(#58892, #59308) the National Key R&D Program(2018YFC1503501),APSCO Earthquake Project:Phase II,ISSI-BJ2019.

ACKNOWLEDGMENTS

In this study, the observed electric field power spectrum data of the CSES supported by the China National Space Administration and China Seismological Bureau are used. We thank all members of the CSES team of the National Institute for Natural Disaster Prevention and Control of the Ministry of Emergency Management for the data provided for this research, especially Dr. Zhang Xuemin of the Prediction Institute of China Earthquake Administration for her valuable opinions.

REFERENCES

Bell, T., Graf, K., Inan, U., Piddyachiy, D., and Parrot, M. (2011). DEMETER Observations of Ionospheric Heating by Powerful VLF Transmitters. *Geophys. Res. Lett.* 38 (11), 47503. doi:10.1029/2011gl047503

Cohen, M. B., and Inan, U. (2012). Terrestrial VLF Transmitter Injection into the Magnetosphere. *J. Geophys. Res. space Phys.* 117 (A8). doi:10.1029/2012ja017992

Cohen, M. B., Lehtinen, N. G., and Inan, U. S. (2012). Models of Ionospheric VLF Absorption of Powerful Ground Based Transmitters. *Geophys. Res. Lett.* 39 (24). doi:10.1029/2012gl054437

Cunningham, G. S., Botek, E., Pierrard, V., Cully, C., and Ripoll, J. F. (2020). Observation of High-energy Electrons Precipitated by NWC Transmitter from PROBA-V low-Earth Orbit Satellite. *Geophys. Res. Lett.* 47 (16), e2020GL089077. doi:10.1029/2020gl089077

Gao, P., Wang, X., Yang, D., Li, W., and Gu, F. (2021). Electric Field Data Storage Experiment of the ZH-1 Satellite. *Prog. Geophys.* 36 (04), 1386. doi:10.6038/pg2021EE0250

Greninger, P. T., and Colman, J. J. (2021). The Seasonality of VLF Attenuation through the Ionosphere Verified by DEMETER Satellite. *JGR Space Phys.* 126 (8), e2020JA028383. doi:10.1029/2020JA028383

Huang, J., Lei, J., Li, S., Zeren, Z., Li, C., Zhu, X., et al. (2018). The Electric Field Detector(EFD) Onboard the ZH-1 Satellite and First Observational Results. *Earth Planet. Phys.* 2 (06), 469–478. doi:10.26464/epp2018045

Ivarsen, M. F., Park, J., Jin, Y., and Clausen, L. B. (2021). Ionospheric Plasma Fluctuations Induced by the NWC Very Low Frequency Signal Transmitter. *J. Geophys. Res. Space Phys.* 126 (5), e2021JA029213. doi:10.1029/2021ja029213

Lehtinen, N. G., and Inan, U. S. (2009). Full-wave Modeling of Transionospheric Propagation of VLF Waves. *Geophys. Res. Lett.* 36 (3), a–n. doi:10.1029/2008GL036535

Li, J. D., Spasojevic, M., Harid, V., Cohen, M. B., Gołkowski, M., and Inan, U. (2014). Analysis of Magnetospheric ELF/VLF Wave Amplification from the Siple Transmitter Experiment. *J. Geophys. Res. Space Phys.* 119 (3), 1837–1850. doi:10.1002/2013ja019513

Li, Z., Li, J., Huang, J., Yin, H., and Jia, J. (2022). Research on Pre-seismic Feature Recognition of Spatial Electric Field Data Recorded by CSES. *Atmosphere* 13 (2), 179. doi:10.3390/atmos13020179

Liao, Z., Wu, B., Shen, X., and Min, M. (2018). Analysis of Ionospheric VTEC Temporal-Spatial Characteristics in Guangxi and Surrounding. *Sci. Surv. Mapp.* 43 (09), 40–45+62. doi:10.16251/j.cnki.1009-2307.2018.09.008

Lu, H., Liu, D., Zhao, S., Ou, M., Huang, J., and Wang, L. (2017). Three-frequency Beacon Data Processing and Product Introduction of Electromagnetic Monitoring Test Satellites." in 2017 China Earth Sciences Joint Academic Annual Conference Proceedings (38)-Special Topics 71: Dynamics of the Inner Magnetosphere, Topic 72: Computational Geophysical Methods and Techniques, Topic 73: Geothermal: "Study" to "Use", Topic 74: Electromagnetic Satellite Observations and Applications, Beijing, 2017.

Ma, M., Lei, J., Li, C., Li, S., Zong, C., Liu, Z., et al. (2018). Design Optimization of Zhangheng-1 Space Electric Field Detector. *Chin. J. Vac. Sci. Technol.* 38 (07), 582–589. doi:10.13922/j.cnki.cjovst.2018.07.06

Meredith, N. P., Horne, R. B., Clilverd, M. A., and Ross, J. P. J. (2019). An Investigation of VLF Transmitter Wave Power in the Inner Radiation Belt and Slot Region. *J. Geophys. Res. Space Phys.* 124 (7), 5246–5259. doi:10.1029/2019ja026715

Němec, F., Pekař, J., and Parrot, M. (2020). NWC Transmitter Effects on the Nightside Upper Ionosphere Observed by a Low-Altitude Satellite. *J. Geophys. Res. Space Phys.* 125 (12), e2020JA028660. doi:10.1029/2020JA028660

Ni, B., Bortnik, J., Thorne, R. M., Ma, Q., and Chen, L. (2013). Resonant Scattering and Resultant Pitch Angle Evolution of Relativistic Electrons by Plasmaspheric Hiss. *J. Geophys. Res. Space Phys.* 118 (12), 7740–7751. doi:10.1002/2013ja019260

Ni, B., Huang, H., Zhang, W., Gu, X., Zhao, H., Li, X., et al. (2019). Parametric Sensitivity of the Formation of Reversed Electron Energy Spectrum Caused by Plasmaspheric Hiss. *Geophys. Res. Lett.* 46 (8), 4134–4143. doi:10.1029/2019gl082032

Potirakis, S., Asano, T., and Hayakawa, M. (2018). Criticality Analysis of the Lower Ionosphere Perturbations Prior to the 2016 Kumamoto (Japan) Earthquakes as Based on VLF Electromagnetic Wave Propagation Data Observed at Multiple Stations. *Entropy* 20 (3), 199. doi:10.3390/e20030199

Shen, X., Yuan, S., Zhang, X., Huang, J., and Zhu, X. (2018). "General Progress of Zhang Heng-1 Satellite Plan," in *2018 Academic Seminar and Seminar on New Technology Advances and Applications of Seismic Electromagnetic Detection by the Seismoelectromagnetics* (Dandong: Professional Committee of China Seismological Society), 62.

Shufan, Z., Li, L., Xuemin, Z., and Xuhui, S. (2016). Full Wave Calculation of Ground-Based VLF Radiation Penetrating into the Ionosphere. *Chin. J. Radio Sci.* 31 (5), 825. doi:10.13443/j.cjors.2016021701

Singh, V., and Obara, Y. (2020). Simultaneous Study of VLF/ULF Anomalies Associated with Earthquakes in Japan. *Open J. Earthq. Res.* 9 (2), 15. doi:10.4236/ojer.2020.92012

Wang, L., Shen, X., Zhang, Y., Zhang, X., Hu, Z., Yan, R., et al. (2016). Developing Progress of China Seismo-Electromagnetic Satellite Project. *Acta Seismol. Sin.* 38 (03), 376. doi:10.11939/jass.2016.03.005

Xu, W. (2016). Signal Processing of Artificial VLF Wave and Study on Electromagnetic Disturbance Characteristics in Space. Dissertation/Master's thesis. Langfang: Institute of Disaster Prevention.

Yang, M., Huang, J., Zhang, X., Shen, X., Wang, L., Zhima, Z., et al. (2018). Analysis on Dynamic Background Field of Ionosphere ELF/VLF Electric Field in Northeast Asia. *Prog. Geophys.* 33 (06), 2285. doi:10.6038/pg2018BB0492

Yao, L., Chen, H., Liu, X., and He, Y. (2011). The Global Characteristics of VLF Electric Field Frequency Spectrumin Ionosphere. *Seismol. Geomagnetic Observation Res.* 32 (04), 27. doi:10.3969/j.issn.1003-3246.2011.04.006

Yuan, S., Zhu, X., and Huang, J. (2018). System Design and Key Technology of China Seismo-Electromagnetic Satellite. *Natl. Remote Sens. Bull.* 22 (S1), 32. doi:10.11834/jrs.20188177

Zhang, X., Qian, J., Shen, X., Liu, J., Wang, Y., and Huang, J. (2020). The Seismic Application Progress in Electromagnetic Satellite and Future Development. *Earthquake* 40 (02), 18. doi:10.12196/j.issn.1000-3274.2020.02.002

Zhao, S., Zhang, X., Zhao, Z., Shen, X., and Zhou, C. (2015). Temporal Variations of Electromagnetic Responses in the Ionosphere Excited by the NWC Communication Station. *Chin. J. Geophys.* 58 (07), 2263. doi:10.6038/cjg20150705

Zhu, J., Liu, Y., Dai, C., and Lin, Z. (2021). *Analysis of the Ionospheric TEC Temporal-Spatial Characteristics in Sichuan and Surrounding Area*. Guilin: Journal of Guilin University of Technology, 1

Zhu, T. (2010). A Preliminary Study on Characteristics of Average Power Spectrum Density of LF/MF Electric Field Observed by DEMETER Satellite. *Acta Seismol. Sin.* 32 (04), 476. doi:10.3969/j.issn.0253-3782.2010.04.010

Conflict of Interest: The authors declare that the research was conducted in the absence of any commercial or financial relationships that could be construed as a potential conflict of interest.

Publisher's Note: All claims expressed in this article are solely those of the authors and do not necessarily represent those of their affiliated organizations, or those of the publisher, the editors, and the reviewers. Any product that may be evaluated in this article, or claim that may be made by its manufacturer, is not guaranteed or endorsed by the publisher.